

A Self Propelled Vortex Dipole Model on a Catenoid

Khushi Banthia¹ and Rickmoy Samanta^{1*}

¹Birla Institute of Technology and Science, Pilani, Hyderabad Campus,
500078, Telangana, India.

*Corresponding author(s). E-mail(s):

rickmoy.samanta@hyderabad.bits-pilani.ac.in;

Contributing authors: f20220982@hyderabad.bits-pilani.ac.in;

Abstract

We investigate vortex dipoles on surfaces of variable negative curvature, focusing on a catenoid of arbitrary throat radius “ a ” as a concrete example. We construct the effective dynamical system taking into account the inter-vortex mutual interactions as well as the self-interaction arising from the geometry of the catenoid. The resulting Hamiltonian dynamics reveals that dipoles move along catenoid geodesics, consistent with recent works, *Gustafsson, J. Nonlinear Sci*, 32, 62 (2022) and *Drivas, Glukhovskiy and Khesin, International Mathematics Research Notices, Volume 2024, Issue 14, Pages 10880–10894* (2024). We utilize the symplectic structure to find a conserved momentum map \mathbf{J} related to the \mathbf{U}_1 symmetry along the azimuthal direction. We explicitly demonstrate the conservation of the Hamiltonian and \mathbf{J} for arbitrary throat radius a . Next, we apply the formalism to demonstrate direct and exchange scattering of classical vortices on the catenoid surface. For comparison, we also demonstrate that chiral pairs with similar initial configurations lead to collective rotational motion (with azimuthal drift) instead of scattering. We finally construct a finite dipole dynamical system on the catenoid, building on the dipole-dipole interactions and demonstrate the emergence of the self propulsion terms to leading order in dipole size. This provides a concrete realization, on a curved minimal surface, of the intuitive statement that a finite dipole *propels* orthogonal to the dipole axis, with a speed modulated by curvature.

Keywords: Differential Geometry, Symplectic Structure, Hamiltonian, Geodesic, Bose Einstein Condensate, Vortex Dipoles, Catenoid

1 Introduction

Vortex dipoles, consisting of two counter-rotating vortices of equal strength, are fundamental self-propelled structures arising in many two-dimensional (2D) and quasi-2D flows. They represent the simplest mode of coherent transport and appear across a wide range of systems, from oceanic and atmospheric vortices to plasmas, superfluids, and Bose–Einstein condensates (BECs). In planar incompressible fluids, classical point-vortex theory [1–4] has been very successful in describing their translational motion, pair interaction, and scattering dynamics. Finite-core and additional viscous effects account for dipole deformation, asymmetric decay, and interaction with walls or background shear [5–8]. Many works have investigated the subtle role of curvature and topology of the underlying fluid domain in dipole and vortex motion in general [9–25], see also [26–28]. When the underlying surface is non-Euclidean, the geometric coupling between curvature and vorticity modifies both the Hamiltonian structure and the resulting trajectories, along with a geometry-dependent interaction kernel. Several recent studies [26–28] have also demonstrated quasi-periodic and chaotic regimes depending on initial separation and curvature. Such analyses underline that curvature acts as an effective external field for vortex motion, breaking the translational symmetry that guarantees uniform propagation in the plane. A significant body of mathematical literature [16, 17, 21–23, 25] has provided analytic arguments towards Kimura’s geodesic conjecture (that tightly bound opposite-sign vortex pairs follow geodesics of the surface), finding that the conjecture holds for infinitesimally close vortex pairs but acquires curvature-dependent corrections at finite separation.

Dipoles have also received enormous interest in many recent condensed matter experiments, particularly the work of Neely *et al.* [30], who observed the controlled nucleation and long-lived propagation of quantized vortex dipoles in an oblate BEC. Freilich *et al.* [31] subsequently developed experimental techniques to extract real-time dipole trajectories, finding connections between microscopic Gross–Pitaevskii dynamics and macroscopic vortex-particle models. More recent experiments [33–36] have developed deeper connections between experiments and theoretical studies in dipoles and vortex clusters in trapped condensates.

In this work, we formulate a dynamical description of vortex dipoles in an incompressible and inviscid fluid domain of variable negative curvature, using the catenoid of arbitrary throat radius a as a canonical example. Starting from the geometry-dependent hydrodynamic Green’s function on the catenoid, we derive the explicit equations of motion for interacting vortices, incorporating both mutual and curvature-induced self-interaction terms. The resulting symplectic structure yields a conserved momentum map associated with the $U(1)$ azimuthal symmetry, and we verify numerically the conservation of both the Hamiltonian and this momentum for arbitrary throat radius. We find that tightly bound dipoles propagate along geodesics of the catenoid, providing explicit confirmation of the geodesic conjecture of Kimura and its recent generalizations to surfaces of variable curvature. We then demonstrate direct and exchange scattering of these dipoles on the catenoid while for co-rotating vortex configurations, we demonstrate collective rotational states (with azimuthal drift). Extending the analysis to finite-sized dipoles, we construct an effective dynamical

system that generalizes the planar dipole models to minimal surfaces of varying negative curvature, yielding analytic expressions for curvature-corrected self-propulsion and orientation dynamics (which are then explicitly validated by numerics). Our work establishes the catenoid as a tractable minimal-surface for analytic studies and provide a geometric basis for future investigations of self-propelled defects, dipoles and vortex clusters (along the lines of Ref. ([28]) on curved manifolds).

We organize the paper as follows: In Sec. (2) we provide the model Hamiltonian system and phase space, along with the associated momentum map corresponding to the azimuthal symmetry of the catenoid. This is followed by a comparison of the vortex dipole motion with catenoid geodesics and numerical checks on the conservation laws for catenoids of arbitrary throat radius in Sec. (3). In Sec. (4) we demonstrate the direct and exchange scattering of classical vortices on the catenoid surface. In contrast, Sec. (5) shows that co-rotating configurations show collective rotational motion with azimuthal drift. We construct a simple model for the dipole motion and orientation dynamics for finite sized dipoles and demonstrate the emergence of the self propulsion terms to leading order in dipole size in Sec. (6). These terms are then explicitly validated by numerics. We conclude in Sec. (7).

2 Model Hamiltonian System and Phase Space

In this section, we review the essential aspects of the catenoid geometry needed to set up the dynamical system for the dipoles, closely following Ref. [16, 17, 21–23, 25]. We consider the catenoid of throat radius $a > 0$ described by

$$X(v, u) = (a \cosh(v/a) \cos u, a \cosh(v/a) \sin u, v), \quad u \in [0, 2\pi], v \in \mathbb{R}.$$

This gives the metric

$$g = \cosh^2\left(\frac{v}{a}\right) dv^2 + a^2 \cosh^2\left(\frac{v}{a}\right) du^2 = \cosh^2\left(\frac{v}{a}\right) (dv^2 + a^2 du^2).$$

with the area element

$$dA = a \cosh^2\left(\frac{v}{a}\right) dv du.$$

Due to the prperiodicity in the azimuthal coordinate u , the hydrodynamic Greens function may be written as

$$G(v_i, u_i; v_j, u_j) = \frac{1}{4\pi} \log\left(\cosh\left(\frac{v_i - v_j}{a}\right) - \cos(u_i - u_j)\right).$$

In order to keep the expressions compact, let us also define

$$F_{ij} := \cosh\left(\frac{v_i - v_j}{a}\right) - \cos(u_i - u_j), \quad h(v) := \cosh\left(\frac{v}{a}\right).$$

For N point vortices with strengths Γ_i at positions (v_i, u_i) , the Hamiltonian governing effective vortex interactions on the catenoid is

$$H = \sum_{1 \leq i < j \leq N} \Gamma_i \Gamma_j G(v_i, u_i; v_j, u_j) - \frac{1}{4\pi} \sum_{i=1}^N \Gamma_i^2 \log h(v_i). \quad (1)$$

The natural symplectic form induced by the area element is

$$\omega = \sum_{i=1}^N \Gamma_i dA_i = \sum_{i=1}^N \Gamma_i a h^2(v_i) dv_i \wedge du_i = \sum_{i=1}^N \Gamma_i a \cosh^2\left(\frac{v_i}{a}\right) dv_i \wedge du_i.$$

The Hamiltonian vector field $X_H = \sum_i (\dot{v}_i \partial_{v_i} + \dot{u}_i \partial_{u_i})$ satisfies $\iota_{X_H} \omega = dH$, which leads us to the Hamilton's equations

$$\Gamma_i a h^2(v_i) \dot{v}_i = \frac{\partial H}{\partial u_i}, \quad \Gamma_i a h^2(v_i) \dot{u}_i = -\frac{\partial H}{\partial v_i}. \quad (2)$$

We thus differentiate the pairwise Green function:

$$\frac{\partial G}{\partial u_i} = \frac{1}{4\pi} \frac{\sin(u_i - u_j)}{F_{ij}}, \quad \frac{\partial G}{\partial v_i} = \frac{1}{4\pi} \frac{1}{a} \frac{\sinh\left(\frac{v_i - v_j}{a}\right)}{F_{ij}}.$$

and the local self interaction

$$\frac{\partial}{\partial v_i} \left(-\frac{1}{4\pi} \Gamma_i^2 \log h(v_i) \right) = -\frac{1}{4\pi} \Gamma_i^2 \cdot \frac{1}{a} \tanh\left(\frac{v_i}{a}\right),$$

to arrive at the final dynamical system,

$$\begin{aligned} \dot{v}_i &= \frac{1}{4\pi a h^2(v_i)} \sum_{\substack{j=1 \\ j \neq i}}^N \Gamma_j \frac{\sin(u_i - u_j)}{F_{ij}}, \\ \dot{u}_i &= -\frac{1}{4\pi a^2 h^2(v_i)} \sum_{\substack{j=1 \\ j \neq i}}^N \Gamma_j \frac{\sinh\left(\frac{v_i - v_j}{a}\right)}{F_{ij}} + \frac{1}{4\pi a^2 h^2(v_i)} \Gamma_i \tanh\left(\frac{v_i}{a}\right) \end{aligned} \quad (3)$$

where

$$h(v) = \cosh\left(\frac{v}{a}\right), \quad F_{ij} = \cosh\left(\frac{v_i - v_j}{a}\right) - \cos(u_i - u_j).$$

The above set of equations will be the governing equations for our analysis. Before analyzing dynamics, let us construct an important conserved quantity that will be useful for us in later sections. First, we note that the catenoid is invariant under the U_1 symmetry under rotations $u \mapsto u + \theta$. The corresponding conserved quantity can

be figured out from the relevant momentum map. Given the symplectic form

$$\omega = \sum_{i=1}^N \Gamma_i a \cosh^2\left(\frac{v_i}{a}\right) dv_i \wedge du_i.$$

we contract ω with the infinitesimal generator $\partial/\partial u$. This gives

$$\iota_{\partial/\partial u} \omega = \sum_{i=1}^N \Gamma_i a \cosh^2\left(\frac{v_i}{a}\right) dv_i = d\left(\sum_{i=1}^N \Gamma_i S(v_i)\right),$$

which implies

$$S'(v) = a \cosh^2(v/a)$$

Hence,

$$S(v) = \int^v a \cosh^2\left(\frac{s}{a}\right) ds = \frac{a}{2}v + \frac{a^2}{4} \sinh\left(\frac{2v}{a}\right).$$

Thus the conserved momentum is

$$J = \sum_{i=1}^N \Gamma_i \left(\frac{a}{2} v_i + \frac{a^2}{4} \sinh\left(\frac{2v_i}{a}\right) \right), \quad \frac{dJ}{dt} = 0. \quad (4)$$

Along with this, we have the usual conservation of the Hamiltonian H defined in Eq. (1). The conservation of J and H will serve as an important diagnostic tools for the subsequent analysis.

3 Investigation of Geodesics

In the study of point vortices on curved surfaces, the so-called *Kimura conjecture* proposes that an infinitesimally close vortex pair of equal and opposite circulations (a vortex dipole) moves, in the vanishing-separation or “dipole” limit, along a geodesic of the underlying surface metric. Kimura first formulated and verified this behaviour on constant-curvature surfaces [12]. Subsequent rigorous work by Boatto and Koiller recast the vortex-pair Hamiltonian on a general Riemannian surface, providing a simple proof of Kimura’s conjecture by showing that the reduced dynamics converge to the geodesic equation [17]. More recently, Gustafsson [23] extended this analysis, deriving directly from the vortex Hamiltonian that, in the dipole limit, the centroid motion satisfies the geodesic equation (with a reparametrised time). The latest advance by Drivas, Glukhovskiy and Khesin [25] generalised the result to asymmetric vortex pairs (non-zero total circulation), showing that such singular pairs follow *magnetic geodesics*; in the special case of vanishing total circulation (a true dipole), one recovers Kimura’s original geodesic motion. With the dynamical equations Eq. (3) at hand, we now proceed to an explicit verification of this result on a catenoid of arbitrary throat radius.

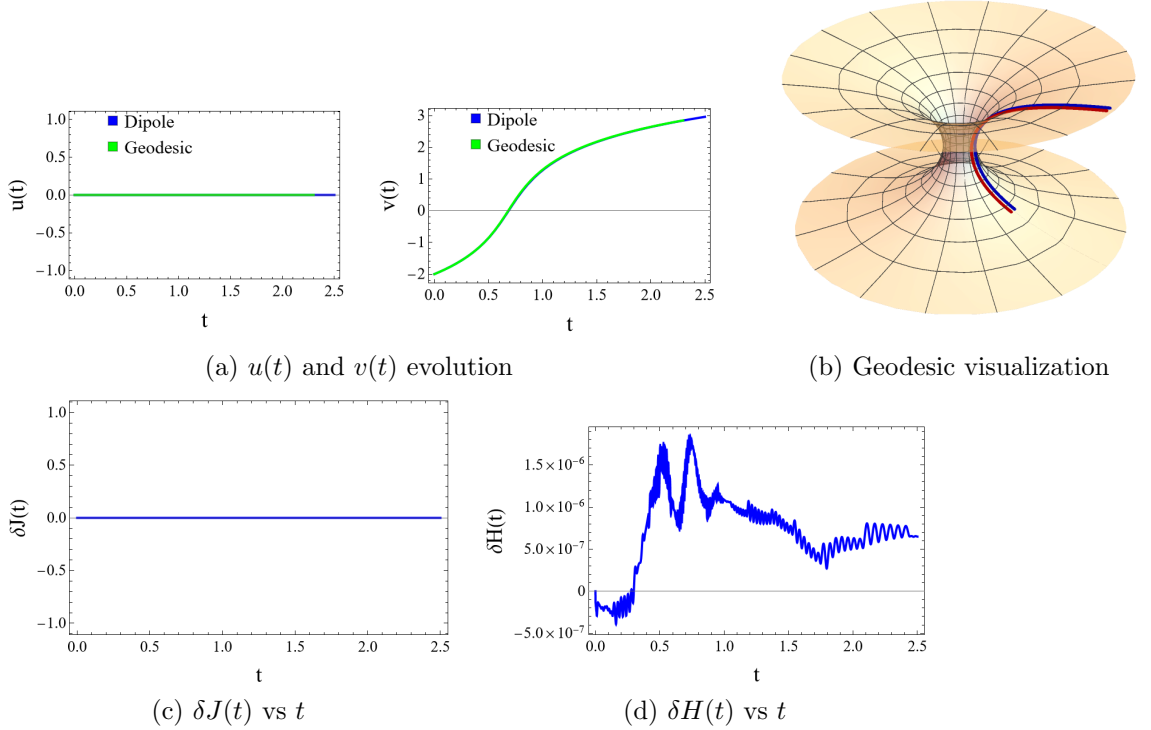


Fig. 1 Meridional geodesic evolution with initial conditions $(u_1, v_1, u_2, v_2) = (\epsilon, -2, -\epsilon, -2)$ with $\epsilon = 0.05$ which yields $J = 0$ (exact) and $\Lambda = 0$ to leading order. Top row: time evolution and geodesic embedding. Bottom row: deviation of conserved quantities δJ and δH . In the (u, v) trajectory plots, the green curve denotes the analytical geodesic solution, while the blue curve shows the corresponding vortex-dipole evolution. For clarity, the geodesic curve is intentionally terminated at an earlier value of the affine parameter so that both trajectories can be visualized distinctly.

For comparison with the dipole trajectory, we need to construct the relevant geodesic equation and solutions, which should be well known. The corresponding nonvanishing Christoffel symbols are

$$\Gamma_{vv}^v = \frac{1}{a} \tanh\left(\frac{v}{a}\right), \quad \Gamma_{uu}^v = -a \tanh\left(\frac{v}{a}\right), \quad \Gamma_{uv}^u = \Gamma_{vu}^u = \frac{1}{a} \tanh\left(\frac{v}{a}\right). \quad (5)$$

Hence, the geodesic equations $\ddot{x}^i + \Gamma_{jk}^i \dot{x}^j \dot{x}^k = 0$ take the explicit form

$$\ddot{v} + \frac{1}{a} \tanh\left(\frac{v}{a}\right) \dot{v}^2 - a \tanh\left(\frac{v}{a}\right) \dot{u}^2 = 0, \quad (6)$$

$$\ddot{u} + \frac{2}{a} \tanh\left(\frac{v}{a}\right) \dot{u} \dot{v} = 0. \quad (7)$$

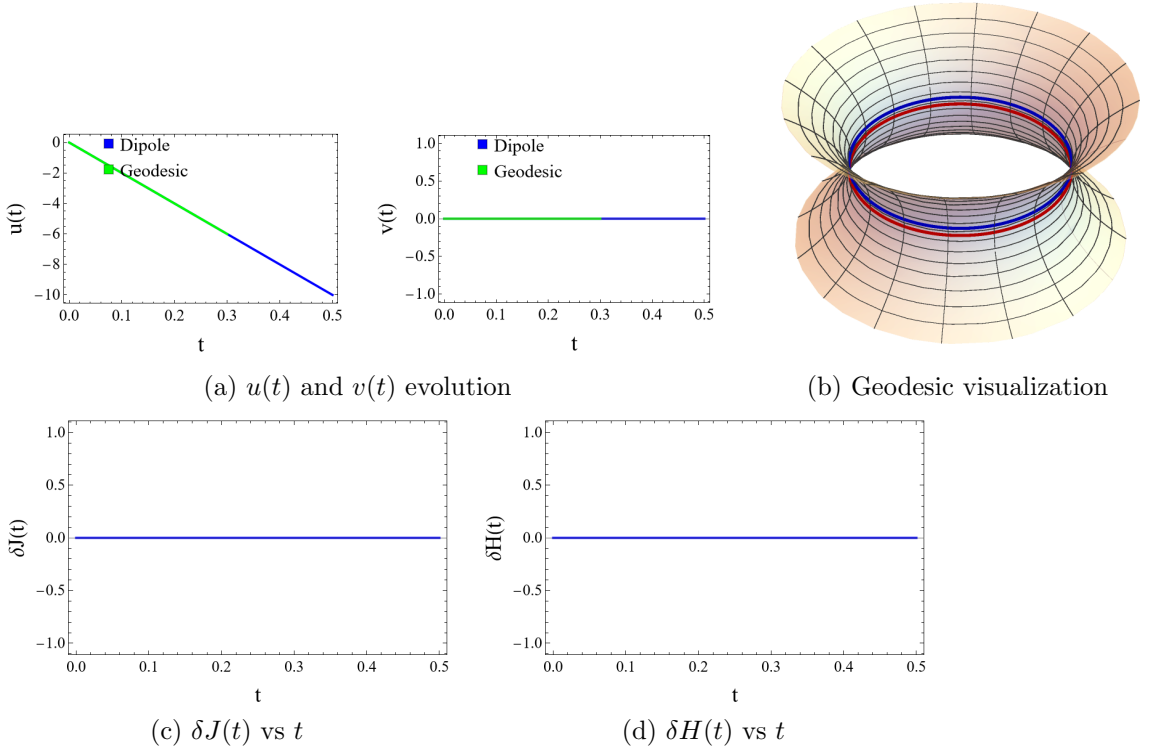


Fig. 2 Critical (neck circle) geodesic evolution for with initial conditions $(u_1, v_1, u_2, v_2) = (0, \epsilon, 0, -\epsilon)$ with $\epsilon = 0.05$ which yields $\Lambda = 1$ to leading order. Top row: time evolution and geodesic embedding. Bottom row: deviation of conserved quantities δJ and δH . In the (u, v) trajectory plots, the green curve denotes the analytical geodesic solution, while the blue curve shows the corresponding vortex-dipole evolution. For clarity, the geodesic curve is intentionally terminated at an earlier value of the affine parameter so that both trajectories can be visualized distinctly.

Equation (7) integrates to

$$p_u = a^2 \cosh^2\left(\frac{v}{a}\right) \dot{u} = \text{const.} \quad (8)$$

Combining (8) with the normalization $2E = \cosh^2(v/a)(\dot{v}^2 + a^2 \dot{u}^2)$ yields

$$\dot{v}^2 = \frac{2E}{\cosh^2(v/a)} - \frac{p_u^2}{a^2 \cosh^4(v/a)}. \quad (9)$$

Introducing the dimensionless ratio

$$\Lambda = \frac{p_u}{a \sqrt{2E}}, \quad (10)$$

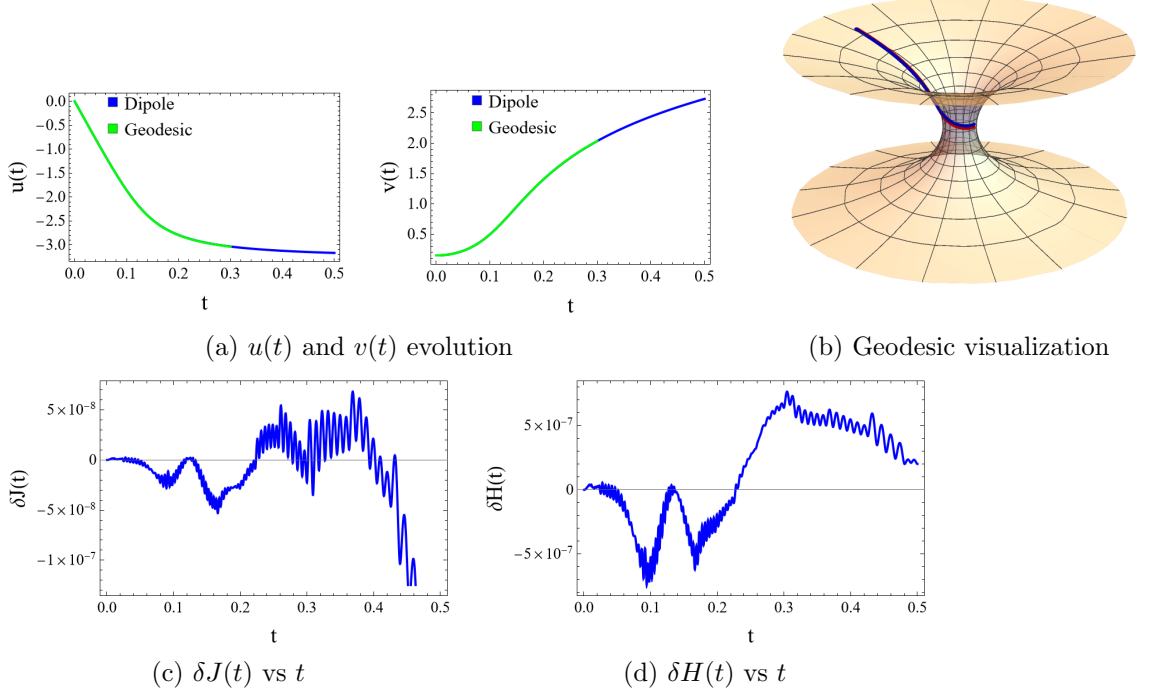


Fig. 3 Trapped one-sided geodesic evolution for with initial conditions $(u_1, v_1, u_2, v_2) = (0, 0.15 + \epsilon, 0, 0.15 - \epsilon)$ with $\epsilon = 0.05$ which yields $\Lambda > 1$ to leading order. Top row: time evolution and geodesic embedding. Bottom row: deviation of conserved quantities δJ and δH . In the (u, v) trajectory plots, the green curve denotes the analytical geodesic solution, while the blue curve shows the corresponding vortex-dipole evolution. For clarity, the geodesic curve is intentionally terminated at an earlier value of the affine parameter so that both trajectories can be visualized distinctly.

one obtains the first-order ‘‘orbit’’ equation,

$$\frac{du}{dv} = \pm \frac{\Lambda}{a \sqrt{\cosh^2 \left(\frac{v}{a} \right) - \Lambda^2}}. \quad (11)$$

One can perform the integral analytically and the solutions are characterized by the parameter Λ . Detailed solutions are constructed in Appendix Sec. (A). Here we collect the main results. Equation (11) admits four qualitatively distinct regimes depending on Λ :

- (i) **Meridional geodesics:** $\Lambda = 0$. Here $du/dv = 0$, so $u = \text{const}$ and the curve runs along a meridian, crossing the neck orthogonally.

(ii) **Trans–throat spirals (Subcritical):** $0 < |\Lambda| < 1$. The square root in (11) is real for all v in this situation, and the geodesic can pass smoothly through the neck,

$$u(v) - u_0 = \pm \Lambda F \left(\arcsin \left(\frac{\sinh(\frac{v}{a})}{\sqrt{\cosh^2(\frac{v}{a}) - \Lambda^2}} \right) \middle| \Lambda^2 \right), \quad (12)$$

where $F(\phi | m)$ is the elliptic integral of the first kind, defined by

$$F(\phi | m) = \int_0^\phi \frac{d\theta}{\sqrt{1 - m \sin^2 \theta}}.$$

For $|\Lambda| < 1$, we have $\cosh^2(\frac{v}{a}) - \Lambda^2 > 0$ for all v , and the formula holds for all v , since

$$\frac{\sinh^2(\frac{v}{a})}{\cosh^2(\frac{v}{a}) - \Lambda^2} \leq \frac{\sinh^2(\frac{v}{a})}{\cosh^2(\frac{v}{a}) - 1} = 1.$$

Alternatively, the solution can be expressed more compactly as

$$u(v) - u_0 = \pm \frac{i\Lambda F \left(\frac{iv}{a}, \frac{1}{1-\Lambda^2} \right)}{\sqrt{1-\Lambda^2}}$$

It can be checked that the above form is real for $|\Lambda| < 1$.

(iii) **Circular neck geodesics (critical):** $|\Lambda| = 1$. The only solution is as $v \rightarrow 0$, we have the circular throat geodesic at $v = 0$:

$$v = 0, \quad u(\tau) = u_0 + \omega\tau, \quad |\Lambda| = 1.$$

(iv) **Trapped one-sided geodesics (supercritical):** $|\Lambda| > 1$. Here the motion is confined to $v \geq v_{tp}$ with $\cosh(v_{tp}/a) = |\Lambda|$. Integration of (11) gives

$$u(v) - u_0 = \pm F \left(\arcsin \left(\frac{\sqrt{\cosh^2(\frac{v}{a}) - \Lambda^2}}{\sinh(\frac{v}{a})} \right) \middle| \frac{1}{\Lambda^2} \right), \quad (13)$$

here once again, $F(\phi | m)$ denotes the elliptic integral of the first kind,

$$F(\phi | m) = \int_0^\phi \frac{d\theta}{\sqrt{1 - m \sin^2 \theta}}.$$

We now wish to construct the dipole trajectories using our vortex equations Eq. (3) specialized to $N = 2$ with counter-rotating unit circulations. It will be advantageous to identify the geodesic parameter Λ in Eq. 10 in terms of the initial data of the dipole, to gain better control on the construction of geodesics belonging to a particular class. Following Drivas, Glukhovskiy and Khesin [25], we can identify the mean motion in

the case of a dipole system consisting of two vortices with strengths $\Gamma_1 = +1$ and $\Gamma_2 = -1$. We define the mean motion of the system by the averages of the azimuthal and radial coordinates, $\bar{u} = \frac{u_1+u_2}{2}$ and $\bar{v} = \frac{v_1+v_2}{2}$, respectively. The corresponding velocities are also defined as the mean values, $\dot{u} = \frac{\dot{u}_1+\dot{u}_2}{2}$ and $\dot{v} = \frac{\dot{v}_1+\dot{v}_2}{2}$. The azimuthal momentum p_u is expressed as:

$$p_u = a^2 \cosh^2 \left(\frac{\bar{v}}{a} \right) \dot{u},$$

and the total energy E is given by:

$$2E = \cosh^2 \left(\frac{\bar{v}}{a} \right) (\dot{v}^2 + a^2 \dot{u}^2).$$

The dimensionless ratio Λ is then defined as:

$$\Lambda = \frac{p_u}{a\sqrt{2E}} = \frac{a^2 \cosh^2 \left(\frac{\bar{v}}{a} \right) \dot{u}}{a\sqrt{\cosh^2 \left(\frac{\bar{v}}{a} \right) (\dot{v}^2 + a^2 \dot{u}^2)}}.$$

This expression for Λ captures the dynamics of the dipole system in terms of the mean positions and velocities of the vortices. For a tight dipole (small $\Delta u, \Delta v$) the effective dipole moving on the catenoid has (we first let $\Delta u \rightarrow 0$ and then $\Delta v \rightarrow 0$)

$$\Lambda = \cosh \left(\frac{\bar{v}}{a} \right) \operatorname{sgn}(\Delta v) + O(\text{dipole size}^2).$$

From the above expression of Λ , it is clear that we will be able to easily engineer the dipole trajectories to follow meridional geodesics, circular neck geodesics as well as trapped one-sided geodesics (supercritical). Figures 1–3 summarize the numerical verification of the geodesic conjecture on the catenoid for three distinct regimes of the dimensionless parameter Λ , which classifies the underlying geodesic family. In Fig. 1, we consider a meridional trajectory corresponding to $\Lambda = 0$ (initial conditions $(u_1, v_1, u_2, v_2) = (\epsilon, -2, -\epsilon, -2)$ with $\epsilon = 0.05$), for which the dipole center moves axially through the throat along $u = \text{const}$. The top panels show the time evolution of $(u(t), v(t))$ and the corresponding embedding of the trajectory on the catenoid, demonstrating agreement between the numerical vortex-pair evolution and the analytical meridional geodesic. In the (u, v) trajectory plots, the green curve denotes the analytical geodesic solution, while the blue curve shows the corresponding vortex-dipole evolution. For clarity, the geodesic curve is intentionally terminated at an earlier value of the affine parameter so that both trajectories can be visualized distinctly in regions where they would otherwise overlap almost exactly. The lower panels plot the errors $\delta H(t) = |H(t) - H(0)|$ and $\delta J(t) = |J(t) - J(0)|$, which remain below 10^{-8} throughout the integration, confirming the exact numerical conservation of both invariants. Figure 2 corresponds to the circular neck or throat geodesic with $\Lambda = 1$, obtained for initial conditions $(u_1, v_1, u_2, v_2) = (0, \epsilon, 0, -\epsilon)$. Here the dipole remains localized near $v = 0$, executing a closed orbit around the neck of the catenoid. The

embedding panel shows the circular motion characteristic of the $|\Lambda| = 1$ family. The conservation plots again show that both H and J are constant to machine precision, demonstrating that the full vortex dynamics respect the Hamiltonian structure. Finally, Fig. 3 depicts the trapped one-sided geodesic for $|\Lambda| > 1$, realized with initial data $(u_1, v_1, u_2, v_2) = (0, 0.15 + \epsilon, 0, 0.15 - \epsilon)$ and $\epsilon = 0.05$. In this regime, the trajectory remains confined to one side of the catenoid, as predicted by the analytic orbit equation (Eq. 11). The numerical path in the (u, v) plane and its catenoid embedding match the theoretical turning point $v_t = a \cosh^{-1} |\Lambda|$, while δH and δJ stay bounded below 10^{-7} , confirming conservation of the Hamiltonian and azimuthal momentum. Taken together, these three representative cases— $\Lambda = 0$, $\Lambda = 1$, and $|\Lambda| > 1$ —provide a direct numerical demonstration that the vortex-dipole trajectories indeed follow the meridional, circular, and trapped geodesics (supercritical) of the catenoid metric, validating the correspondence and the conservation properties of the Hamiltonian system.

4 Demonstration of Direct and Exchange Scattering of Dipoles

We now demonstrate that the dipole dynamics described by Eq. (3) on the catenoid admit the two fundamental types of two-body scattering processes: the *direct* and *exchange* scattering of vortex dipoles. Study of such collisions is interesting in the context of BEC formation, see Ref. [30, 31] in curved trap geometries. In contrast to the flat case, here the Gaussian curvature of the surface modifies both the impact and the post-collision trajectories, providing a geometric control parameter for the scattering.

Direct scattering.

Figure 4 shows the direct-scattering event for two oppositely oriented dipoles initialized near the catenoid throat. The initial configuration is described by the coordinates $\{(0, \epsilon), (\epsilon, 0), (1 - \delta, 1), (1, 1 - \delta)\}$ with strengths $\Gamma = \{-1, 1, 1, -1\}$. The small parameters are chosen to introduce a small off-axis asymmetry $\epsilon = 0.07$, $\delta = 0.03$, and the final integration time $t_f = 0.5$. The left figure depicts the vortex trajectories in the (u, v) -plane and the right figure shows the scattering on the catenoid surface. As the two dipoles approach one another from opposite sides, they interact briefly and then separate, each preserving its internal identity and orientation. The (u, v) projection displays the characteristic right-angle scattering familiar from planar hydrodynamics, now modulated by the non-uniform metric factor $h(v) = \cosh(v/a)$. Throughout the encounter the Hamiltonian and azimuthal momentum remain conserved to within a relative error of 10^{-7} , confirming that the event is an exact Hamiltonian flow on the catenoid.

Exchange scattering.

Figure 5 depicts the exchange-scattering regime obtained in the initial locations of the dipoles by removing the small off-axis symmetry of the direct scattering channel ie. $\epsilon = \delta = 0.05$ and $t_f = 0.5$. Here the dipoles collide obliquely and exchange partners:

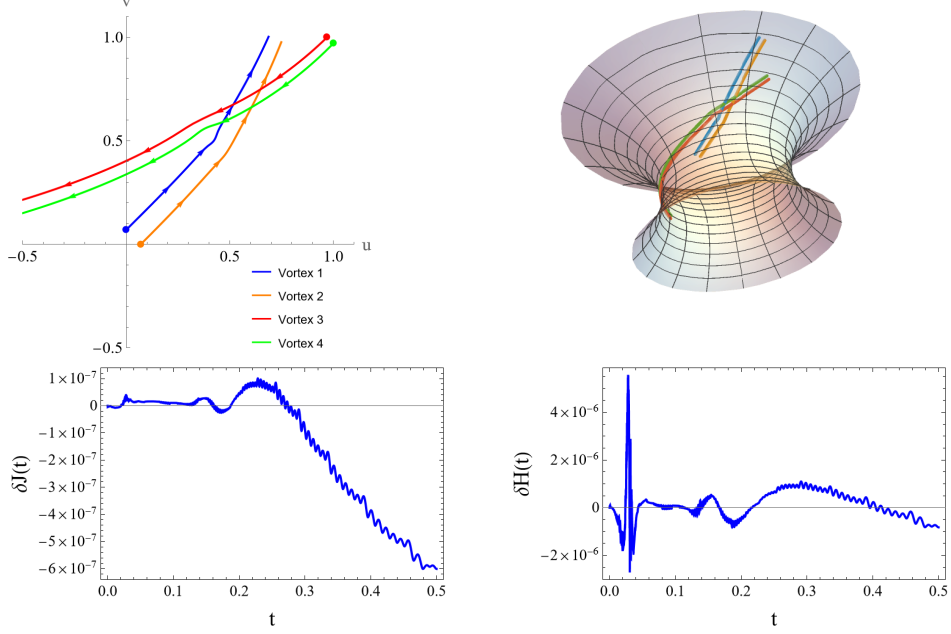


Fig. 4 Direct scattering of two dipoles on a catenoid surface. The dipoles are initialized symmetrically about the diagonal with a small offset, with the first dipole located near the origin in the (u, v) coordinate plane and the second approaching from the vicinity of $(1, 1)$. A small parameter $\epsilon = 0.07, \delta = 0.03$ defines the initial configuration $\{(0, \epsilon), (\epsilon, 0), (1 - \delta, 1), (1, 1 - \delta)\}$, with vortex strengths $\Gamma = \{-1, 1, 1, -1\}$. The top panels show the trajectories at the final integration time $t_f = 0.5$, both in the (u, v) coordinate plane and mapped onto the catenoid surface. The lower panels display the temporal evolution of the conserved quantities J and H , demonstrating their numerical conservation throughout the simulation.

after the encounter, each vortex becomes bound to the opposite sign vortex from the other dipole, forming two new dipoles that propagate away from the throat region. The embedded-surface trajectories reveal a distinct crossing and recombination pattern of the vortex lines. Once again, both H and J remain conserved to numerical precision, demonstrating that the exchange process, although topologically nontrivial, still corresponds to a symplectic dynamics in the four-vortex phase space.

Taken together, Figs. 4 and 5 establish that the catenoid supports the full range of classical two-dipole scattering behaviours. In both cases, conservation of the Hamiltonian and azimuthal momentum to machine accuracy demonstrates the exact symplectic nature of the evolution governed by Eq. (3). These results extend the canonical planar picture of vortex-dipole collisions to curved manifolds, showing explicitly how the geometry of the catenoid—through its negative Gaussian curvature—acts as a tunable control of the scattering angles. A detailed study of all scattering channels on the catenoid is left for a more detailed future communication.

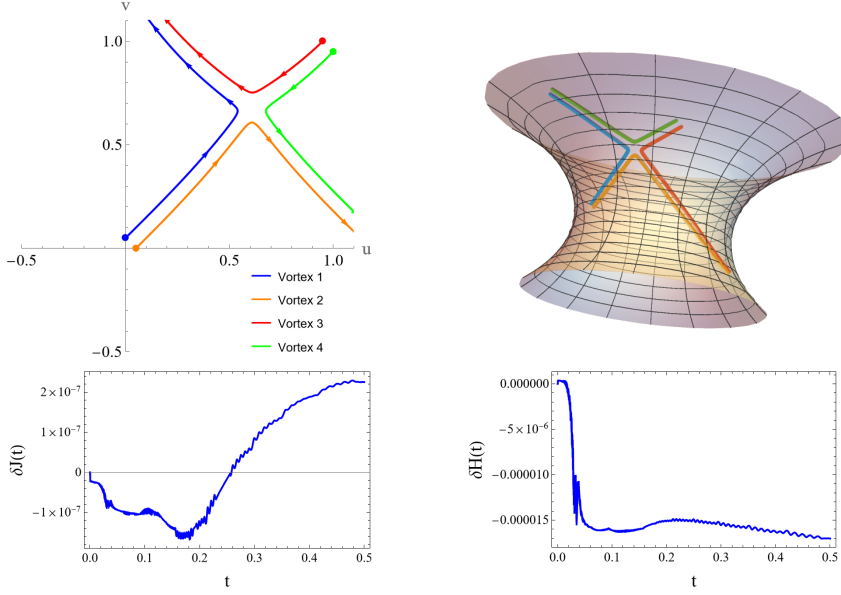


Fig. 5 Exchange scattering of two dipoles on a catenoid surface. The dipoles are initialized symmetrically about the diagonal, with the first dipole located near the origin in the (u, v) coordinate plane and the second approaching from the vicinity of $(1, 1)$. A small parameter $\epsilon = \delta = 0.05$ defines the initial configuration $\{(0, \epsilon), (\epsilon, 0), (1 - \delta, 1), (1, 1 - \delta)\}$, with vortex strengths $\Gamma = \{-1, 1, 1, -1\}$. The top panels show the trajectories at the final integration time $t_f = 0.5$, both in the (u, v) coordinate plane and mapped onto the catenoid surface. The lower panels display the temporal evolution of the conserved quantities J and H , demonstrating their numerical conservation throughout the simulation.

5 Demonstration of collective rotation for Co-rotating pairs

We now explore the same configurations as the dipoles in the last section but with co-rotating vortices. We demonstrate that this leads to collective rotational dynamics along with a simple azimuthal drift. Figures 6 and 7 present representative examples of this co-rotating regime. Figure 6 shows the evolution of symmetric pairs of vortices with same circulation $\Gamma = +1$, initially placed in the same configuration as the dipoles in Fig. (4) and the integration time $t_f = 10$. The panels display the vortex trajectories in (u, v) plane and also on the catenoid. The vortices execute uniform counter-rotating motion about the neck, maintaining a nearly constant separation and forming steady co-rotating pairs with azimuthal drift. The embedding view highlights the circular orbits wrapping around the throat, while the (u, v) plot exhibits the oscillations in height v , induced by the metric factor $h(v) = \cosh(v/a)$. The examples of Figs. 6 and 7 together demonstrate the existence of stable, collectively rotating vortex pairs on negatively curved surfaces. Unlike the dipole motion discussed in Sec. 4, where opposite circulations lead to translation and scattering, same-sign pairs undergo rigid rotation about the surface neck, driven by the intrinsic curvature of the catenoid.

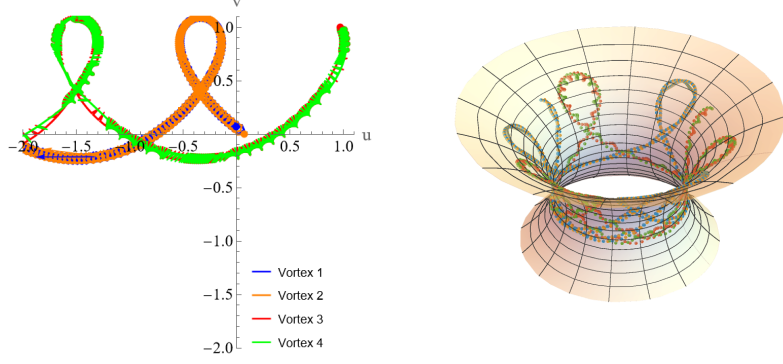


Fig. 6 Co-rotating four-vortex dynamics on a catenoid surface. The vortices are initialized in the direct-scattering configuration $\{(0, \epsilon), (\epsilon, 0), (1 - \delta, 1), (1, 1 - \delta)\}$ with identical circulations $\Gamma_i = 1$, $\epsilon = 0.07$, $\delta = 0.03$, and $t_f = 10$. Unlike the dipole configurations, the uniform circulation leads to a collective rotational motion (with azimuthal drift) and intricate looping trajectories, shown in Cartesian grid (left) and on the catenoid surface (right).

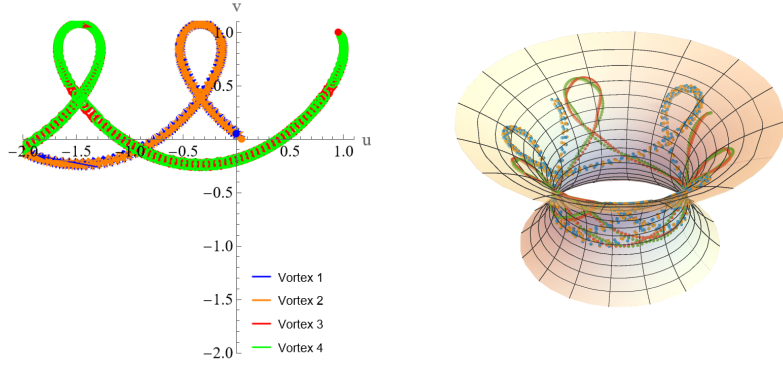
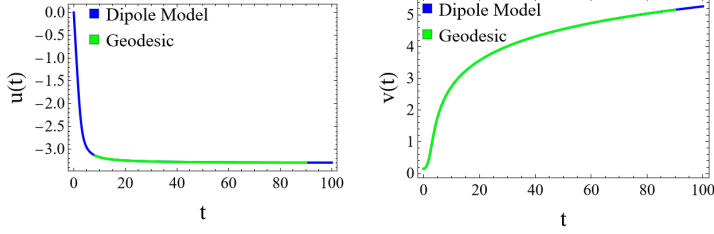


Fig. 7 Co-rotating four-vortex dynamics on a catenoid surface. The vortices are initialized in the exchange-scattering configuration $\{(0, \epsilon), (\epsilon, 0), (1 - \delta, 1), (1, 1 - \delta)\}$ with identical circulations $\Gamma_i = 1$, $\epsilon = 0.05$, $\delta = 0.05$, and $t_f = 10$. Unlike the dipole configurations, the uniform circulation leads to a collective rotational motion (with azimuthal drift) and intricate looping trajectories, shown in Cartesian grid (left) and on the catenoid surface (right).

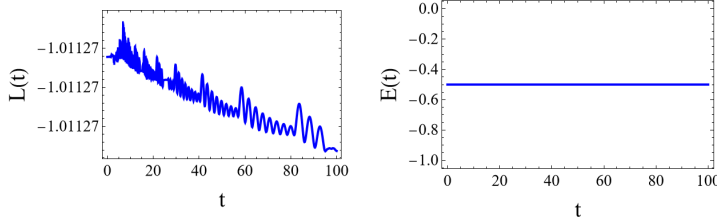
6 Construction of the finite-dipole dynamical system and self-propulsion terms

Having understood the dynamical content of Eq. (3), we now wish to construct a simple model of interacting finite-sized dipoles moving on the catenoid surface, keeping in mind the BEC dipoles in curved trap geometries. Starting from the metric and local orthonormal frame, we derive the curvature-corrected self-propulsion terms and the equations governing the coupled evolution of the dipole centre and orientation. Given the catenoid metric is

$$ds^2 = a^2 h(v)^2 du^2 + h(v)^2 dv^2, \quad h(v) = \cosh\left(\frac{v}{a}\right), \quad (14)$$



(a) Comparison of $u(t)$ and $v(t)$ between dipole model and geodesic motion



(b) Conserved quantities $L(t)$ and $E(t)$ along the geodesic

Fig. 8 Comparison between the finite-dipole model and the corresponding geodesic motion on a catenoid. (**Top**) Evolution of the dipole coordinates $u(t)$ and $v(t)$ obtained from the self-propelled dipole model (blue) and the analytical geodesic motion (green). (**Bottom**) The angular momentum $L(t)$ and energy $E(t)$ remain constant, confirming that the reduced dipole model preserves the expected invariants of geodesic motion.

we first construct the orthonormal basis vectors

$$\hat{e}_u = \frac{1}{ah} \partial_u, \quad \hat{e}_v = \frac{1}{h} \partial_v. \quad (15)$$

The Levi–Civita connection one–form in this orthonormal frame is

$$\omega(\partial_u) = \tanh(v/a), \quad \omega(\partial_v) = 0, \quad (16)$$

so that a tangent vector parallel transported along a trajectory with velocity components (\dot{u}, \dot{v}) rotates at the rate

$$\omega(X) = \tanh(v/a) \dot{u}. \quad (17)$$

For convenience, let us recall that for N point vortices with circulations Γ_i , the equations of motion in (u, v) coordinates are

$$\dot{v}_i = \frac{1}{4\pi a h_i^2} \sum_{j \neq i} \Gamma_j \frac{\sin(u_i - u_j)}{F_{ij}},$$

$$\dot{u}_i = -\frac{1}{4\pi a^2 h_i^2} \sum_{j \neq i} \Gamma_j \frac{\sinh\left(\frac{v_i - v_j}{a}\right)}{F_{ij}} + \frac{1}{4\pi a^2 h_i^2} \Gamma_i \tanh\left(\frac{v_i}{a}\right), \quad (18a)$$

where

$$F_{ij} = \cosh\left(\frac{v_i - v_j}{a}\right) - \cos(u_i - u_j), \quad h_i = \cosh(v_i/a).$$

Each dipole n consists of two vortices of equal and opposite circulation, $\Gamma_{n,+} = +1$ and $\Gamma_{n,-} = -1$. The two vortices are separated by a small geodesic distance ℓ_n along the tangent

$$\hat{\mathbf{t}}_n = \cos \alpha_n \hat{e}_u + \sin \alpha_n \hat{e}_v,$$

where α_n is the orientation angle measured from the u -direction. To first order in ℓ_n , the coordinates of the \pm vortices are

$$u_{n,\pm} = u_n \pm \frac{\ell_n}{2ah_n} \cos \alpha_n, \quad v_{n,\pm} = v_n \pm \frac{\ell_n}{2h_n} \sin \alpha_n, \quad h_n = h(v_n). \quad (19)$$

Self Propulsion

The self-propelled motion of a dipole arises from the mutual advection of its two constituent vortices. The velocity of the $+$ vortex due to its $-$ partner is

$$\dot{u}_{n,+}^{(\text{partner})} = -\frac{\Gamma_{n,-}}{4\pi a^2 h(v_{n,+})^2} \frac{\sinh\left(\frac{v_{n,+} - v_{n,-}}{a}\right)}{F_{(n,+)(n,-)}} + \frac{1}{4\pi a^2 h(v_{n,+})^2} \Gamma_{n,+} \tanh\left(\frac{v_{n,+}}{a}\right), \quad (20a)$$

$$\dot{v}_{n,+}^{(\text{partner})} = \frac{\Gamma_{n,-}}{4\pi a h(v_{n,+})^2} \frac{\sin(u_{n,+} - u_{n,-})}{F_{(n,+)(n,-)}}, \quad (20b)$$

and similarly with $+$ replaced by $-$. Averaging these two velocities gives the self-propulsion velocity of the dipole centre:

$$\begin{aligned} \dot{u}_n^{(\text{self})} &= \frac{1}{8\pi a^2} \left[\frac{\sinh\left(\frac{v_{n,+} - v_{n,-}}{a}\right)}{h(v_{n,+})^2 F_{(n,+)(n,-)}} - \frac{\sinh\left(\frac{v_{n,-} - v_{n,+}}{a}\right)}{h(v_{n,-})^2 F_{(n,-)(n,+)}} + \frac{\tanh\left(\frac{v_{n,+}}{a}\right)}{h(v_{n,+})^2} - \frac{\tanh\left(\frac{v_{n,-}}{a}\right)}{h(v_{n,-})^2} \right], \\ \dot{v}_n^{(\text{self})} &= -\frac{1}{8\pi a} \left[\frac{\sin(u_{n,+} - u_{n,-})}{h(v_{n,+})^2 F_{(n,+)(n,-)}} + \frac{\sin(u_{n,-} - u_{n,+})}{h(v_{n,-})^2 F_{(n,-)(n,+)}} \right]. \end{aligned} \quad (21)$$

Using the displacements from Eq. (19),

$$\Delta u_n = u_{n,+} - u_{n,-} = \frac{\ell_n}{ah_n} \cos \alpha_n, \quad \Delta v_n = v_{n,+} - v_{n,-} = \frac{\ell_n}{h_n} \sin \alpha_n,$$

we obtain to leading order in ℓ_n , the self-propulsion velocity components are (obtained in *Mathematica*)

$$\begin{aligned}\dot{u}_i^{(\text{self})} &= \frac{\mu_i \operatorname{sech}\left(\frac{v_i}{a}\right) \sin \alpha_i}{2a\pi \ell_i} + O(\ell_i), \\ \dot{v}_i^{(\text{self})} &= -\frac{\mu_i \cos \alpha_i \operatorname{sech}\left(\frac{v_i}{a}\right)}{2\pi \ell_i} + O(\ell_i),\end{aligned}\tag{22}$$

where μ_i represent the strength of dipole i . Note that the self propulsion described by the above equation is orthogonal to the dipole axis, as expected. The full expressions are carried out in *Mathematica* and presented in Appendix Sec (C).

External advection

Using the compact notation

$$F_{(n,\pm)(m,r)} = \cosh\left(\frac{v_{n,\pm} - v_{m,r}}{a}\right) - \cos(u_{n,\pm} - u_{m,r}).$$

the velocity of the $+$ vortex of dipole n induced by all other dipoles $m \neq n$ is

$$\begin{aligned}\dot{u}_{n,+}^{(\text{ext})} &= -\frac{1}{4\pi a^2 h_n^2} \sum_{m \neq n} \sum_{r=\pm} \Gamma_{m,r} \left[\frac{\sinh\left(\frac{v_{n,+} - v_{m,r}}{a}\right)}{F_{(n,+)(m,r)}} \right], \\ \dot{v}_{n,+}^{(\text{ext})} &= \frac{1}{4\pi a h_n^2} \sum_{m \neq n} \sum_{r=\pm} \Gamma_{m,r} \left[\frac{\sin(u_{n,+} - u_{m,r})}{F_{(n,+)(m,r)}} \right]\end{aligned}$$

and similarly for the negative vortex. Note that since we have already incorporated the vortex self-interaction term in the self propulsion, we exclude this contribution in the external advection. Averaging over the two vortices in the n -th dipole, we have the total external contribution to the mean advection:

$$\begin{aligned}\dot{u}_n^{(\text{ext})} &= \frac{1}{8\pi a h_n^2} \sum_{m \neq n} \sum_{r=\pm} \Gamma_{m,r} \left[\frac{\sin(u_{n,+} - u_{m,r})}{F_{(n,+)(m,r)}} + \frac{\sin(u_{n,-} - u_{m,r})}{F_{(n,-)(m,r)}} \right], \\ \dot{v}_n^{(\text{ext})} &= -\frac{1}{8\pi a^2 h_n^2} \sum_{m \neq n} \sum_{r=\pm} \Gamma_{m,r} \left[\frac{\sinh\left(\frac{v_{n,+} - v_{m,r}}{a}\right)}{F_{(n,+)(m,r)}} + \frac{\sinh\left(\frac{v_{n,-} - v_{m,r}}{a}\right)}{F_{(n,-)(m,r)}} \right],\end{aligned}\tag{24a}$$

with

$$F_{(n,\pm)(m,r)} = \cosh\left(\frac{v_{n,\pm} - v_{m,r}}{a}\right) - \cos(u_{n,\pm} - u_{m,r}).$$

Evolution of the orientation angle.

The orientation α_n evolves due to (i) the differential velocity of the two vortices (local shear), (ii) external torques from other dipoles and (iii) the geometric parallel transport

on the curved surface, see more details on orientation dynamics in Appendix Sec. (B). The first contribution is given by

$$\dot{\alpha}_n^{(\text{self})} = \frac{\mu_n}{\ell_n} (-\sin \alpha_n A_n + \cos \alpha_n B_n),$$

$$A_n = a \left[\cosh\left(\frac{v_{n,+}}{a}\right) u_{n,+}^{(\text{partner})} - \cosh\left(\frac{v_{n,-}}{a}\right) u_{n,-}^{(\text{partner})} \right],$$

$$B_n = \cosh\left(\frac{v_{n,+}}{a}\right) v_{n,+}^{(\text{partner})} - \cosh\left(\frac{v_{n,-}}{a}\right) v_{n,-}^{(\text{partner})}.$$

The second contribution due to the external torques from the other dipoles is given by

$$\dot{\alpha}_n^{(\text{ext})} = \frac{\mu_n}{\ell_n} (-\sin \alpha_n A_n^{(\text{ext})} + \cos \alpha_n B_n^{(\text{ext})}),$$

$$A_n^{(\text{ext})} = a \left[\cosh\left(\frac{v_{n,+}}{a}\right) u_{n,+}^{(\text{ext})} - \cosh\left(\frac{v_{n,-}}{a}\right) u_{n,-}^{(\text{ext})} \right],$$

$$B_n^{(\text{ext})} = \cosh\left(\frac{v_{n,+}}{a}\right) v_{n,+}^{(\text{ext})} - \cosh\left(\frac{v_{n,-}}{a}\right) v_{n,-}^{(\text{ext})}.$$

Along with this, we also need to add the contribution to rotational contribution due to parallel transport, more details on this appears in Appendix Sec. (B). The complete rotation rate is given by the sum of all three contributions:

$$\dot{\alpha}_n = \dot{\alpha}_n^{(\text{self})} + \dot{\alpha}_n^{(\text{ext})} + \tanh\left(\frac{v_n}{a}\right) \dot{u}_n. \quad (25)$$

The self term vanishes at leading order since the two partner vortices generate equal and opposite velocities, producing translation without rotation. The subleading correction is (obtained in *Mathematica*)

$$\dot{\alpha}_i^{(\text{self})} = -\frac{\mu_i \operatorname{sech}^3\left(\frac{v_i}{a}\right) \sin \alpha_i \tanh\left(\frac{v_i}{a}\right) \ell_i}{24 a^3 \pi} \left(\cos^2 \alpha_i - 6 \sin^2 \alpha_i + 6 \sin^2 \alpha_i \tanh^2\left(\frac{v_i}{a}\right) \right) + O(\ell_i^2).$$

The full expressions are carried out in *Mathematica* and presented in Appendix Sec (C).

Full dipole dynamics.

Combining Eqs. (21), (24) and (25), the complete dynamical system for N dipoles on the catenoid is

$$\dot{u}_n = \dot{u}_n^{(\text{self})} + \dot{u}_n^{(\text{ext})},$$

$$\dot{v}_n = \dot{v}_n^{(\text{self})} + \dot{v}_n^{(\text{ext})},$$

$$\dot{\alpha}_n = \dot{\alpha}_n^{(\text{self})} + \dot{\alpha}_n^{(\text{ext})} + \tanh\left(\frac{v_n}{a}\right) \dot{u}_n.$$
(26)

To summarize the origin of the different contributions,

- $\dot{u}_n^{(\text{self})}, \dot{v}_n^{(\text{self})}, \dot{\alpha}_n^{(\text{self})}$ are the curvature-corrected self-propulsion terms from Eq. (21);
- $\dot{u}_n^{(\text{ext})}, \dot{v}_n^{(\text{ext})}, \dot{\alpha}_n^{(\text{ext})}$ are the external interaction terms from Eq. (24);
- the final term in the orientation evolution represents the parallel-transport correction to the rotational velocity on the surface.

Figure 8 provides a numerical validation of the finite-dipole system derived above, keeping only the leading self-propulsion terms of Eq. (22). The dipole is initialized such that $\Lambda > 1$ so that we are in the supercritical class of trapped one-sided geodesics. In panel (a) we compare the time evolution of the dipole centre $(u(t), v(t))$ obtained from the full self-propelled dipole equations (26) (blue curves) with the corresponding catenoid geodesic constructed from the same initial data (green curves). The two trajectories are almost indistinguishable over the entire integration interval, the geodesic curve is intentionally truncated in time to make this overlap visible. The agreement improves further if we go beyond the truncated expressions of Eq. (22) and use the full expressions from Appendix Sec. (C). This agreement shows that, once the leading curvature-corrected self-propulsion terms (21) are included (as well as the curvature mediated orientation rate), the finite dipole indeed moves along the geodesic of the supercritical class. Panel (b) displays the the geodesic conserved quantities, $L(t)$ and $E(t)$. Both errors stay below 10^{-7} , confirming that the numerical scheme preserves the Lagrangian structure and that the key terms in (26) (self-propulsion and parallel transport contribution to orientation dynamics) are essential ingredients to build the finite-sized dipole system on the catenoid, and on any curved surface in general.

7 Conclusion

In this work we developed and tested a geometric description of vortex dipoles on a surface of variable negative curvature, taking the catenoid of throat radius a as a canonical example. Starting from the catenoid metric and its induced symplectic structure, we derived the point-vortex Hamiltonian in closed form, including the curvature-dependent self term $-\frac{1}{4\pi}\Gamma_i^2 \log h(v_i)$. This allowed us to identify the natural $U(1)$ symmetry associated with azimuthal rotations and to construct the corresponding momentum map

$$J = \sum_{i=1}^N \Gamma_i \left(\frac{a}{2} v_i + \frac{a^2}{4} \sinh \frac{2v_i}{a} \right),$$

which we verified numerically to be conserved together with the Hamiltonian for arbitrary throat radius. These invariants then served as stringent diagnostics for all subsequent simulations in our work. A central result of the paper is the explicit confirmation of Kimura's geodesic conjecture on a nontrivial minimal surface. By specializing the Hamiltonian dynamics to a two-vortex system of opposite circulations and passing to mean variables (\bar{u}, \bar{v}) , we showed that tightly bound dipoles propagate along catenoid geodesics, with the single dimensionless parameter

$$\Lambda = \frac{a^2 \cosh^2(\bar{v}/a) \dot{u}}{a \sqrt{\cosh^2(\bar{v}/a) (\dot{v}^2 + a^2 \dot{u}^2)}}$$

classifying the orbits into meridional ($\Lambda = 0$), circular neck ($|\Lambda| = 1$), and trapped one-sided (supercritical) ($|\Lambda| > 1$) families. Figures 1–3 demonstrated that the dipole trajectories obtained from the full vortex equations lie on top of the corresponding geodesic solutions, and that the relative errors in both H and J remain at or below 10^{-7} .

We then used the same Hamiltonian framework to study genuinely dynamical phenomena that do not appear in the infinitesimal dipole limit. In Sec. 4 we showed that the catenoid supports both *direct* and *exchange* scattering of classical vortex dipoles: depending on a small asymmetry in the initial impact geometry, the colliding vortex pairs either retain their identity or exchange partners. The fact that H and J stay conserved through the entire collision confirms that the scattering is mediated purely by curvature and not by numerical artefacts. In Sec. 5 we contrasted this with the case of same-sign vortices, where we found long-lived, collectively rotating configurations (co-rotating pairs/four-vortex states) with overall azimuthal drift, accompanied by conservation of H and J .

Finally, in Sec. 6 we constructed an explicit *finite dipole* dynamical system on the catenoid. By displacing the two vortices of a dipole by $\pm\ell_n/2$ along a tangent direction α_n , inserting these positions into the vortex equations, and averaging, we obtained closed expressions for the curvature-corrected self-propulsion,

$$\dot{u}_n^{(\text{self})} \sim \frac{\text{sech}(v_n/a) \sin \alpha_n}{\ell_n}, \quad \dot{v}_n^{(\text{self})} \sim -\frac{\text{sech}(v_n/a) \cos \alpha_n}{\ell_n},$$

together with an evolution equation for the orientation that contains both shear-induced and parallel-transport terms. This provides a concrete realization, on a curved minimal surface, of the intuitive statement that a finite dipole *propels* orthogonal to the direction of its axis, with a speed modulated by curvature.

There are several natural directions for future work. An immediate extension of the work presented here will be to study the scattering a self propelled dipole with co-rotating cluster of vortices, which is also interesting in the context of the BEC experiments. Dynamics of vortex clusters on surfaces of varying negative curvature also will be reported in future, in line with Ref. ([28]). On the mathematical aspects, the current work can be generalized in several directions. First, the present analysis was carried out on the catenoid because of its analytic tractability; it would be interesting to repeat the construction on other minimal or negatively curved surfaces (e.g. pseudospherical patches, corrugated films) to see how universal the self-propulsion terms are. Second, our finite-dipole model keeps only the leading order in the separation ℓ ; incorporating the next order would provide a controlled way to quantify the generic behavior of a large many body system of dipoles on the catenoid, using our full expressions in Appendix (C). Third, the catenoid offers a natural setting for studying vortex interactions in curved BEC trap geometries, where the present formulation could be considered as a simplified version of the full Gross–Pitaevskii simulations. Finally, since the momentum map J is explicit, one can use this to attempt a more systematic classification of scattering channels on the catenoid, which we leave for a detailed communication in future.

In summary, our work shows that: (i) vortex dipoles on a catenoid follow geodesics classified by a single parameter Λ ; (ii) the full point-vortex Hamiltonian conserves both H and the azimuthal momentum map J for arbitrary throat radius; (iii) Varying negative curvature surfaces like the catenoid admit direct and exchange scattering of dipoles; and (iv) a simple finite-sized dipole model is constructed that yields curvature-corrected self-propulsion and orientation dynamics, explicitly validated by numerics. We hope this work will motivate further analytical and numerical studies of vortex matter on curved manifolds, where geometry can be used as a tunable control parameter for vortex transport.

Acknowledgements. We are very thankful to Suryateja Gavva, Naomi Oppenheimer and Haim Diamant. R.S is supported by DST INSPIRE Faculty fellowship, India (Grant No.IFA19-PH231). Both authors acknowledge support from NFSG and OPERA Research Grant from Birla Institute of Technology and Science, Pilani (Hyderabad Campus).

Declarations

The data that supports the findings of this study are available within the article.

Appendix A Solution of the geodesic orbit integrals

In this appendix we solve explicitly the first-order “orbit” equation for geodesic trajectories on the catenoid

$$\frac{du}{dv} = \pm \frac{\Lambda}{a \sqrt{\cosh^2\left(\frac{v}{a}\right) - \Lambda^2}}, \quad (\text{A1})$$

where $a > 0$ is the catenoid throat radius and Λ is a constant fixed by the conserved quantities defined in the main text. The sign \pm corresponds to the two orientation choices of the curve. The structure of the solution depends on whether $|\Lambda| > 1$ or $|\Lambda| < 1$, so we treat these cases separately. Throughout, $F(\phi|m)$ denotes the incomplete elliptic integral of the first kind,

$$F(\phi|m) := \int_0^\phi \frac{d\theta}{\sqrt{1 - m \sin^2 \theta}}.$$

We first remove the length scale a from the independent variable via

$$x := \frac{v}{a} \quad \implies \quad dv = a dx.$$

Then (A1) becomes

$$\frac{du}{dx} = \pm \frac{\Lambda}{\sqrt{\cosh^2 x - \Lambda^2}},$$

and the problem reduces to the single integral

$$u(x) - u_0 = \pm \Lambda \int \frac{dx}{\sqrt{\cosh^2 x - \Lambda^2}}, \quad (\text{A2})$$

where u_0 is an integration constant. We now evaluate (A2) in the two regimes, such that we can bring the integrals to standard elliptic integral forms in the respective regimes.

$|\Lambda| > 1$ (supercritical case)

When $|\Lambda| > 1$ we write

$$\cosh^2 x - \Lambda^2 = \sinh^2 x - (\Lambda^2 - 1).$$

Let us introduce

$$\alpha^2 := \Lambda^2 - 1 > 0.$$

Then

$$u - u_0 = \pm \Lambda \int \frac{dx}{\sqrt{\sinh^2 x - \alpha^2}}.$$

Set $z = \sinh x$. Then

$$u - u_0 = \pm \Lambda \int \frac{dz}{\sqrt{1+z^2} \sqrt{z^2 - \alpha^2}}.$$

We now introduce

$$z = \frac{\alpha}{\sqrt{1-y^2}}, \quad |y| < 1.$$

such that the integral becomes

$$u - u_0 = \pm \Lambda \int \frac{dy}{\sqrt{1-y^2} \sqrt{\Lambda^2 - y^2}}.$$

We set $y = \sin \phi$. Then

$$u - u_0 = \pm \int \frac{d\phi}{\sqrt{1 - \frac{1}{\Lambda^2} \sin^2 \phi}} = \pm F\left(\phi \mid \frac{1}{\Lambda^2}\right).$$

We express ϕ in terms of the original variable v . Tracing back the substitutions, the solution can be written as

$$u(v) - u_0 = \pm F\left(\arcsin \frac{\sqrt{\cosh^2(\frac{v}{a}) - \Lambda^2}}{\sinh(\frac{v}{a})} \mid \frac{1}{\Lambda^2}\right), \quad |\Lambda| > 1. \quad (\text{A3})$$

For $|\Lambda| > 1$ the radicand $\cosh^2(v/a) - \Lambda^2$ is non-negative only if

$$\cosh\left(\frac{v}{a}\right) \geq |\Lambda| \implies |v| \geq v_{\text{tp}} := a \operatorname{arcosh} |\Lambda|.$$

Thus the trajectory has a turning point at $v = \pm v_{\text{tp}}$, as expected for this regime.

$|\Lambda| < 1$ (subcritical case)

When $|\Lambda| < 1$ we instead use

$$\cosh^2 x - \Lambda^2 = \sinh^2 x + (1 - \Lambda^2).$$

Let us now define

$$\beta^2 := 1 - \Lambda^2 \in (0, 1),$$

so that (A2) becomes

$$u - u_0 = \pm \Lambda \int \frac{dx}{\sqrt{\sinh^2 x + \beta^2}}.$$

We change variables

$$\sinh x = \beta \sinh t.$$

Hence

$$u - u_0 = \pm \Lambda \int \frac{dt}{\sqrt{1 + \beta^2 \sinh^2 t}}.$$

Let $y = \tanh t$ such that we have

$$u - u_0 = \pm \Lambda \int \frac{dy}{\sqrt{1 - y^2} \sqrt{1 - \Lambda^2 y^2}}.$$

Finally we set $y = \sin \phi$ again. Then

$$u - u_0 = \pm \Lambda \int \frac{d\phi}{\sqrt{1 - \Lambda^2 \sin^2 \phi}} = \pm \Lambda F(\phi | \Lambda^2).$$

Similar to the supercritical case, we express ϕ in terms of v , leading us to

$$u(v) - u_0 = \pm \Lambda F\left(\arcsin \frac{\sinh\left(\frac{v}{a}\right)}{\sqrt{\cosh^2\left(\frac{v}{a}\right) - \Lambda^2}} \middle| \Lambda^2\right), \quad |\Lambda| < 1. \quad (\text{A4})$$

For $|\Lambda| < 1$ we have

$$\cosh^2\left(\frac{v}{a}\right) - \Lambda^2 > 0 \quad \text{for all } v \in \mathbb{R},$$

so, unlike the $|\Lambda| > 1$ case, there is no turning point and the solution is real for all v .

Moreover,

$$\frac{\sinh^2\left(\frac{v}{a}\right)}{\cosh^2\left(\frac{v}{a}\right) - \Lambda^2} \leq \frac{\sinh^2\left(\frac{v}{a}\right)}{\cosh^2\left(\frac{v}{a}\right) - 1} = 1,$$

so the argument of the $\arcsin(\cdot)$ in (A4) indeed lies in $[-1, 1]$ for all v . *Mathematica* may return for (A4) the equivalent form

$$u(v) - u_0 = \pm \frac{i\Lambda}{\sqrt{1 - \Lambda^2}} \text{EllipticF}\left(\frac{iv}{a}, \frac{1}{1 - \Lambda^2}\right),$$

which is related to (A4) by the standard imaginary-argument identity for the elliptic integral. We have preferred the manifestly real expressions (A3) and (A4).

Appendix B Orientation dynamics

We derive here the evolution equation governing the orientation of a finite vortex dipole on a curved surface, with the catenoid as our primary example. Let the right- and left-hand vortices of the dipole, with circulations $+\Gamma$ and $-\Gamma$, occupy positions

$$\mathbf{x}_+ = \mathbf{x}_d + \frac{1}{2}\mathbf{d}, \quad \mathbf{x}_- = \mathbf{x}_d - \frac{1}{2}\mathbf{d}, \quad (\text{B5})$$

where \mathbf{x}_d denotes the dipole center and \mathbf{d} is the separation vector lying in the local tangent plane. The dipole length is $\ell = |\mathbf{d}|$, and its orientation is represented by the unit vector

$$\hat{\mathbf{e}}_{\parallel} = \frac{\mathbf{d}}{\ell}, \quad \hat{\mathbf{e}}_{\perp} = \hat{\mathbf{n}} \times \hat{\mathbf{e}}_{\parallel}, \quad (\text{B6})$$

where $\hat{\mathbf{n}}$ is the unit normal to the surface. Differentiating the dipole vector gives

$$\dot{\mathbf{d}} = \dot{\mathbf{x}}_+ - \dot{\mathbf{x}}_- = \dot{\ell} \hat{\mathbf{e}}_{\parallel} + \ell \dot{\hat{\mathbf{e}}}_{\parallel}. \quad (\text{B7})$$

Under the finite-dipole constraint the separation magnitude remains constant ($\dot{\ell} = 0$), so

$$\dot{\hat{\mathbf{e}}}_{\parallel} = \frac{1}{\ell}(\dot{\mathbf{x}}_+ - \dot{\mathbf{x}}_-) = \frac{1}{\ell} \Delta \mathbf{V}, \quad (\text{B8})$$

where $\Delta \mathbf{V}$ is the relative velocity of the two vortices in the tangent plane. The orientation of the dipole is described by an angle α , measured from the local meridional (u) direction. By construction,

$$\dot{\hat{\mathbf{e}}}_{\parallel} = \dot{\alpha} \hat{\mathbf{e}}_{\perp}. \quad (\text{B9})$$

Projecting the previous expression onto $\hat{\mathbf{e}}_{\perp}$ yields the general law

$$\dot{\alpha} = \frac{1}{\ell} \hat{\mathbf{e}}_{\perp} \cdot (\dot{\mathbf{x}}_+ - \dot{\mathbf{x}}_-). \quad (\text{B10})$$

Equation (B10) states that the instantaneous angular velocity of the dipole axis is determined by the component of the differential vortex velocity perpendicular to the dipole separation.

We now compute the contribution from parallel transport to the rotation rate. We introduce the orthonormal coframe $\theta^1 = a h(v) du$ and $\theta^2 = h(v) dv$, so that $ds^2 = (\theta^1)^2 + (\theta^2)^2$. The Cartan structure equations $d\theta^1 + \omega \wedge \theta^2 = 0$ and $d\theta^2 - \omega \wedge \theta^1 = 0$

determine the Levi–Civita connection one–form ω . Since $d\theta^1 = -ah'(v) du \wedge dv$ and $d\theta^2 = 0$, one finds $\omega = (ah'/h) du$. Using $h'(v) = a^{-1} \sinh(v/a)$ gives

$$\omega = \tanh\left(\frac{v}{a}\right) du. \quad (\text{B11})$$

Evaluating this on a trajectory $X = \dot{u} \partial_u + \dot{v} \partial_v$ yields the instantaneous rotation rate of a parallel–transported vector:

$$\omega(X) = \tanh\left(\frac{v}{a}\right) \dot{u}. \quad (\text{B12})$$

Hence only motion around the azimuthal direction (u) generates a local rotation of transported vectors, with magnitude set by the geometric factor $\tanh(v/a)$. Consequently, Eq. (B10) reduces to

$$\dot{\alpha} = \frac{1}{\ell} \hat{\mathbf{e}}_{\perp} \cdot (\dot{\mathbf{x}}_+ - \dot{\mathbf{x}}_-) + \tanh\left(\frac{v}{a}\right) \dot{u}_d, \quad (\text{B13})$$

which coincides with Eq. (6.13) of the main text. The additional term proportional to $\tanh(v/a)$ represents the geometric rotation of the local basis vectors as the dipole center moves along the surface. Equations (B10) and (B13) show that the dipole orientation evolves due to *differential advection* between its two constituent vortices. The curvature of the catenoid introduces an effective torque that rotates the dipole axis even when the relative velocity vanishes in flat-space coordinates. In the planar limit $a \rightarrow \infty$, the curvature term disappears, and the expression reduces to the classical finite-dipole result of Aref [1] and Saffman [2].

Appendix C Full expressions of self-propulsion terms

Here we provide the full expressions for the self-propulsion velocity and rotation rate as described in the main text.

$$\begin{aligned} \dot{u}_i^{(\text{self})} = & -\frac{1}{8a^2\pi \left(\cos\left(\frac{\ell_i \cos \alpha_i \operatorname{sech}\left(\frac{v_i}{a}\right)}{a}\right) - \cosh\left(\frac{\ell_i \operatorname{sech}\left(\frac{v_i}{a}\right) \sin \alpha_i}{a}\right) \right)} \\ & \times \left\{ \mu_i \operatorname{sech}^2\left(\frac{v_i - \frac{1}{2}\ell_i \operatorname{sech}\left(\frac{v_i}{a}\right) \sin \alpha_i}{a}\right) \sinh\left(\frac{\ell_i \operatorname{sech}\left(\frac{v_i}{a}\right) \sin \alpha_i}{a}\right) \right. \\ & \times \left[\cos\left(\frac{\ell_i \cos \alpha_i \operatorname{sech}\left(\frac{v_i}{a}\right)}{a}\right) - \cosh\left(\frac{\ell_i \operatorname{sech}\left(\frac{v_i}{a}\right) \sin \alpha_i}{a}\right) \tanh\left(\frac{v_i - \frac{1}{2}\ell_i \operatorname{sech}\left(\frac{v_i}{a}\right) \sin \alpha_i}{a}\right) \right] \\ & + \mu_i \operatorname{sech}^2\left(\frac{v_i + \frac{1}{2}\ell_i \operatorname{sech}\left(\frac{v_i}{a}\right) \sin \alpha_i}{a}\right) \sinh\left(\frac{\ell_i \operatorname{sech}\left(\frac{v_i}{a}\right) \sin \alpha_i}{a}\right) \end{aligned}$$

$$\begin{aligned}
& \times \left[-\cos\left(\frac{\ell_i \cos \alpha_i \operatorname{sech}\left(\frac{v_i}{a}\right)}{a}\right) + \cosh\left(\frac{\ell_i \operatorname{sech}\left(\frac{v_i}{a}\right) \sin \alpha_i}{a}\right) \tanh\left(\frac{v_i + \frac{1}{2} \ell_i \operatorname{sech}\left(\frac{v_i}{a}\right) \sin \alpha_i}{a}\right) \right] \Bigg\} \\
& \quad (C14)
\end{aligned}$$

$$\dot{v}_i^{(\text{self})} = \frac{\mu_i \left\{ \operatorname{sech}^2\left(\frac{v_i - \frac{1}{2} \ell_i \operatorname{sech}\left(\frac{v_i}{a}\right) \sin \alpha_i}{a}\right) + \operatorname{sech}^2\left(\frac{v_i + \frac{1}{2} \ell_i \operatorname{sech}\left(\frac{v_i}{a}\right) \sin \alpha_i}{a}\right) \right\} \sin\left(\frac{\ell_i \cos \alpha_i \operatorname{sech}\left(\frac{v_i}{a}\right)}{a}\right)}{8a\pi \left(\cos\left(\frac{\ell_i \cos \alpha_i \operatorname{sech}\left(\frac{v_i}{a}\right)}{a}\right) - \cosh\left(\frac{\ell_i \operatorname{sech}\left(\frac{v_i}{a}\right) \sin \alpha_i}{a}\right) \right)}$$

$$\begin{aligned}
\dot{\alpha}_i^{(\text{self})} = & \frac{1}{4a\ell_i\pi \left(\cos\left(\frac{\ell_i \cos \alpha_i \operatorname{sech}\left(\frac{v_i}{a}\right)}{a}\right) - \cosh\left(\frac{\ell_i \operatorname{sech}\left(\frac{v_i}{a}\right) \sin \alpha_i}{a}\right) \right)} \\
& \times \mu_i \left\{ -\operatorname{sech}\left(\frac{v_i - \frac{1}{2} \ell_i \operatorname{sech}\left(\frac{v_i}{a}\right) \sin \alpha_i}{a}\right) \right. \\
& \quad \cdot \left[\cos \alpha_i \sin\left(\frac{\ell_i \cos \alpha_i \operatorname{sech}\left(\frac{v_i}{a}\right)}{a}\right) + \sin \alpha_i \sinh\left(\frac{\ell_i \operatorname{sech}\left(\frac{v_i}{a}\right) \sin \alpha_i}{a}\right) \right] \\
& \quad + \left(\cos\left(\frac{\ell_i \cos \alpha_i \operatorname{sech}\left(\frac{v_i}{a}\right)}{a}\right) - \cosh\left(\frac{\ell_i \operatorname{sech}\left(\frac{v_i}{a}\right) \sin \alpha_i}{a}\right) \right) \\
& \quad \cdot \sin \alpha_i \tanh\left(\frac{v_i - \frac{1}{2} \ell_i \operatorname{sech}\left(\frac{v_i}{a}\right) \sin \alpha_i}{a}\right) \\
& \quad + \operatorname{sech}\left(\frac{v_i + \frac{1}{2} \ell_i \operatorname{sech}\left(\frac{v_i}{a}\right) \sin \alpha_i}{a}\right) \\
& \quad \cdot \left[\cos \alpha_i \sin\left(\frac{\ell_i \cos \alpha_i \operatorname{sech}\left(\frac{v_i}{a}\right)}{a}\right) + \sin \alpha_i \sinh\left(\frac{\ell_i \operatorname{sech}\left(\frac{v_i}{a}\right) \sin \alpha_i}{a}\right) \right] \\
& \quad + \left(-\cos\left(\frac{\ell_i \cos \alpha_i \operatorname{sech}\left(\frac{v_i}{a}\right)}{a}\right) + \cosh\left(\frac{\ell_i \operatorname{sech}\left(\frac{v_i}{a}\right) \sin \alpha_i}{a}\right) \right) \\
& \quad \cdot \sin \alpha_i \tanh\left(\frac{v_i + \frac{1}{2} \ell_i \operatorname{sech}\left(\frac{v_i}{a}\right) \sin \alpha_i}{a}\right) \Bigg\}. \\
& \quad (C15)
\end{aligned}$$

References

- [1] H. Aref, *Integrable, chaotic, and turbulent vortex motion in two-dimensional flows*, *Annu. Rev. Fluid Mech.* **15** (1983) 345–389.
- [2] P. G. Saffman, *Vortex Dynamics* (Cambridge Univ. Press, 1993).
- [3] C. C. Lin, *On the motion of vortices in two dimensions: I. Existence of the Kirchhoff–Routh function*, *Proc. Natl. Acad. Sci. USA* **27** (1941) 570–575.
- [4] C. C. Lin, *On the motion of vortices in two dimensions: II. Some further investigations on the Kirchhoff–Routh function*, *Proc. Natl. Acad. Sci. USA* **27** (1941) 575–577.
- [5] I. Delbende and M. Rossi, *The dynamics of a viscous vortex dipole*, *Phys. Fluids* **21** (2009) 053605.
- [6] D. Dehtryiov, K. Hourigan and M. C. Thompson, *Direct numerical simulation of a counter-rotating vortex pair interacting with a wall*, *J. Fluid Mech.* **884** (2020) A36.
- [7] J. B. Flór and G. J. F. van Heijst, *An experimental study of dipolar vortex structures in a stratified fluid*, *J. Fluid Mech.* **279** (1994) 101–133.
- [8] A. K. Hinds, S. J. Thorpe and R. W. Griffiths, *Laboratory study of vortex dipoles interacting with step topography*, *J. Geophys. Res.* **114** (2009) C06006.
- [9] V. A. Bogomolov, *Dynamics of vorticity on a sphere*, *Fluid Dyn.* **12** (1977) 863–870.
- [10] D. Hally, *Stability of streets of vortices on surfaces of revolution with a reflection symmetry*, *J. Math. Phys.* **21** (1980) 211–217.
- [11] Y. Kimura and H. Okamoto, *Vortex motion on a sphere*, *J. Phys. Soc. Jpn.* **56** (1987) 4203–4206.
- [12] Y. Kimura, *Vortex motion on surfaces with constant curvature*, *Proc. R. Soc. A* **455** (1999) 245–259.
- [13] R. Kidambi and P. K. Newton, *Streamline topologies for integrable vortex motion on a sphere*, *Physica D* **140** (2000) 95–125.
- [14] R. Kidambi and P. K. Newton, *Point vortex motion on a sphere with solid boundaries*, *Phys. Fluids* **12** (2000) 581–588.
- [15] D. G. Crowdy and J. Marshall, *Analytical formulae for the Kirchhoff–Routh path function in multiply connected domains*, *Proc. R. Soc. A* **461** (2005) 2477–2501.

- [16] S. Boatto and J. Koiller, *Vortices on closed surfaces*, in *Geometry, Mechanics, and Dynamics: The Legacy of Jerry Marsden*, (Springer, New York, 2008) pp. 185–199.
- [17] J. Koiller and S. Boatto, *Vortex pairs on surfaces*, *J. Nonlinear Sci.* **19** (2009) 1–25.
- [18] A. M. Turner, V. Vitelli and D. R. Nelson, *Vortices on curved surfaces*, *Rev. Mod. Phys.* **82** (2010) 1301–1348.
- [19] A. V. Borisov and I. S. Mamaev, *Dynamics of point vortices on a sphere in the case of two vortex pairs*, *Regul. Chaotic Dyn.* **19** (2014) 287–304.
- [20] R. Reuther and A. Voigt, *The interplay of curvature and vortices in flow on curved surfaces*, *Multiscale Model. Simul.* **13** (2014) 632–643.
- [21] S. Boatto and J. Koiller, *Vortices on closed surfaces*, *Fields Inst. Commun.* **73** (2015) 185–237.
- [22] D. G. Dritschel and S. Boatto, *The motion of point vortices on closed surfaces*, *Proc. R. Soc. A* **471** (2015) 20140890.
- [23] B. Gustafsson, *Vortex pairs and dipoles on closed surfaces*, *J. Nonlinear Sci.* **32** (2022) 62.
- [24] K. Lydon, A. Coffey and G. Bewley, *Dipole dynamics in the point-vortex model*, *Phys. Fluids* **35** (2023) 087101.
- [25] T. D. Drivas, D. Glukhovskiy and B. Khesin, *Singular vortex pairs follow magnetic geodesics*, *Int. Math. Res. Not.* **2024** (2024) rnae096.
- [26] R. Samanta and N. Oppenheimer, *Vortex flows and streamline topology in curved biological membranes*, *Phys. Fluids* **33** (2021) 092111.
- [27] U. Maurya, S. T. Gavva, A. Saha and R. Samanta, *Vortex dynamics in tubular fluid membranes*, *Phys. Fluids* **37** (2025) 073109.
- [28] K. R. Aswathy, U. Maurya, S. T. Gavva and R. Samanta, *Dynamics of vortex clusters on a torus*, *Phys. Fluids* **37** (2025) 093324.
- [29] M. A. Caracanhas, V. S. Bagnato and F. E. A. dos Santos, *Superfluid vortex dynamics on axisymmetric surfaces*, *Phys. Rev. A* **105** (2022) 013318.
- [30] T. W. Neely, E. C. Samson, A. S. Bradley, M. J. Davis and B. P. Anderson, *Observation of vortex dipoles in an oblate Bose–Einstein condensate*, *Phys. Rev. Lett.* **104** (2010) 160401.

- [31] D. V. Freilich, D. M. Bianchi, A. M. Kaufman, T. K. Langin and D. S. Hall, *Real-time dynamics of single vortex lines and vortex dipoles in a Bose-Einstein condensate*, *Science* **329** (2010) 1182–1185.
- [32] S. Middelkamp *et al.*, *Guiding-center dynamics of vortex dipoles in Bose-Einstein condensates*, *Phys. Rev. A* **84** (2011) 011605.
- [33] S. J. Rooney, P. B. Blakie, B. P. Anderson and A. S. Bradley, *Suppression of Kelvin-wave decay in oblate Bose-Einstein condensates*, *Phys. Rev. A* **84** (2011) 023637.
- [34] R. H. Goodman, P. G. Kevrekidis and R. Carretero-González, *Dynamics of vortex dipoles in anisotropic traps*, *SIAM J. Appl. Dyn. Syst.* **14** (2015) 699–729.
- [35] A. C. White, C. F. Barenghi and N. P. Proukakis, *Vortices and turbulence in trapped atomic condensates*, *J. Phys. B: At. Mol. Opt. Phys.* **47** (2014) 235301.
- [36] G. W. Stagg, N. G. Parker and C. F. Barenghi, *Generation and decay of two-dimensional quantum turbulence in trapped Bose-Einstein condensates*, *J. Phys. B: At. Mol. Opt. Phys.* **47** (2014) 095304.